www.sciencemag.org/content/355/6324/507/suppl/DC1

Supplementary Material for

Ultrastructural evidence for synaptic scaling across the wake/sleep cycle

Luisa de Vivo, Michele Bellesi, William Marshall, Eric A. Bushong, Mark H. Ellisman, Giulio Tononi,* Chiara Cirelli*

*Corresponding author. Email: ccirelli@wisc.edu (C.C.); gtononi@wisc.edu (G.T.)

Published 3 February 2017, *Science* **355**, 507 (2017)
DOI: 10.1126/science.aah5982

This PDF file includes:

Materials and Methods

Animals. Three groups of B6.Cg-Tg(Thy1-YFP)16Jrs/J mice were used (YFP-H, Jackson laboratory; ~1month old; 4 mice / group). Previous confocal and two-photon *in vivo* microscopy experiments have characterized development-related changes in spine density in YFP-H mice (*36*). Moreover, electroencephalographic (EEG) analysis of sleep and wake patterns has been extensively done in this strain (*36, 37*). Mice were single-housed in environmentally controlled recording chambers with free access to food and water (12 h:12 h light-dark cycle; lights on at 08:00). At the beginning of each dark period a running wheel and 1-2 novel objects were introduced in each recording chamber, to ensure enriched housing conditions and facilitate the light/dark entrainment of the rest/activity cycle. Running wheels and novel objects were removed during the light period, except in the case of EW mice (see below). All animal procedures and experimental protocols followed the National Institutes of Health Guide for the Care and Use of Laboratory Animals and were approved by the licensing committee. All animal facilities were reviewed and approved by the institutional animal care and use committee (IACUC) of the University of Wisconsin-Madison, and were inspected and accredited by association for assessment and accreditation of laboratory animal care (AAALAC).

Analysis of behavioral states and experimental groups. Behavioral states were determined by continuous monitoring with infrared cameras, to avoid possible tissue damage and inflammation due to the implant of electrodes for polysomnographic recording. In previous experiments we found that video-monitoring consistently estimates total sleep time with ≥90% accuracy, although it cannot distinguish NREM sleep from REM sleep (*38*). Motor activity was quantified by custom-made video-based motion detection algorithms, as detailed in previous studies (*39*). Sleep/wake criteria for the experimental groups were as follows: spontaneously awake (SW) mice were euthanized during the dark phase (~2-3:30 am) at the end of a long period of wake (> 1 hour, interrupted by periods of sleep of <5 min), and after spending at least 70% of the previous 6–7 hours awake. Sleeping (S) mice were euthanized during the light period (~2-4:45 pm), at the end of a long period of sleep (> 45 min, interrupted by periods of wake of <4 min), and after spending at least 75% of the previous 6–7 hours asleep. EW (enforced wake) mice were kept awake during the first part of the light period (6-7 hours) by exposure to novel objects and running wheel and by tapping on the cage whenever the animals appeared drowsy. EW mice were never disturbed when spontaneously awake, grooming, feeding or drinking, and were euthanized at the same circadian time as the S group (2-4:45pm). The night prior to the experiment EW mice showed the expected sleep/wake pattern: they were spontaneously awake for most of the first part of the night (% of the first 6h of the night spent awake; 62.8 ± 5.6, mean ± std), while during the second half of the dark period they slept

roughly half of the time (% of the last 6h of the night spent awake; 49.8 ± 8.5). Thus, the duration of almost continuous wake in the 6-7 hours before collection was not very different between SW and EW mice. "Quality" of wake, however, may have differed between the two groups: EW mice were exposed to a greater number of novel objects but were also sleepy and less willing to explore than SW mice, and may have experienced short microsleeps and/or "local sleep" (40) during the period of sleep deprivation.

Tissue Preparation for Electron Microscopy. Under deep anesthesia (3% isoflurane), mice were perfused intracardially with a solution of 0.05 M phosphate buffered saline (PBS) followed by 2.5% glutaraldehyde and 2% paraformaldehyde dissolved in 0.1M sodium cacodylate buffer (41°C and pH 7.4). Brains were removed and kept in the same fixative overnight at 4°C. Tissue slices (120 μm) were cut on a vibratome and kept in a cryoprotectant solution until the day of processing. Small blocks of tissue (1mm^2) from primary motor cortex (M1, 1.85 mm anterior to bregma, 1.5 mm lateral) and primary somatosensory cortex (S1, 1mm posterior to bregma, 3.5 mm lateral) were excised under a stereomicroscope and stained as described in (*41*). Staining was performed blind to experimental condition. Briefly, the tissue was rinsed in cacodylate buffer, incubated for 1 h on ice with a solution of 1.5% potassium ferrocyanide/2% osmium tetroxide, and exposed to a solution of 1% thiocarbohydrazide for 20 min at room temperature. Afterwards, the sample was placed in 2% osmium tetroxide for 30 min and incubated overnight with 1% uranyl acetate at 4°C. The following day, the tissue was stained with a solution of lead aspartate for 30 min at 60°C (pH 5.5) and dehydrated using ice-cold solutions of freshly prepared 35%, 50%, 75%, 80%, 90%, 95%, and 100% ethanol. The sample was then placed in propylene oxide for 10 min and impregnated with 25%, 50%, 75% Durcupan ACM resin mixed with propylene oxide (2 h each). The tissue was then placed in fresh 100% Durcupan several times, flat embedded with ACLAR embedding film and kept in a 60°C oven for 48–72 h. After polymerization, the stained tissue was excised under a stereomicroscope and attached on the tip of a metal pin using conductive epoxy resin. The block of tissue was trimmed and coated with silver paint to minimize specimen charging during imaging.

Image acquisition. Images were obtained using a ΣIGMA^{TM} VP field emission scanning electron microscoscope equipped with 3View® technology, and a backscattered electron detector. In serial block-face scanning electron microscopy (SBEM), serial images are obtained by scanning the face of an unsliced block of tissue placed inside the microscope, then cutting off ultrathin slices using an automated microtome within the instrument. The newly exposed surface of the sliced block is rescanned until a stack of images is obtained. In this study serial images were acquired using an aperture of 30μm, high vacuum, acceleration voltage of 1.5-2kV, image size of 5000 by 5000 pixels, image resolution (xy plane) of 5.9nm, and ultrathin sections were cut at a nominal thickness of 25-50nm. Two stacks of ~500 images each were

acquired per mouse (10,878-21,756 μm^3), one in layer 2 of M1 and another in layer 2 of S1. Images were Gaussian filtered and automatically aligned using the open source software Fiji (*42*). Average actual section thickness for each stack was estimated using the cylindrical diameters method as previously described (*43*), and did not differ across the 3 conditions (52.4 ± 10.5 nm for the S group, 54.7 ± 4.8 nm for the SW group, and 51.4 ± 10.3 nm for the EW group; Kruskal-Wallis p=0.68). Dendritic segments and all their protrusions were segmented manually in TrakEM2 (*44*) by seven trained annotators who were blind to experimental condition. We randomly selected spiny dendritic segments that could be followed within the stack and whose diameter ranged between 0.5 and 1.7μm. In layer 2, densely spiny dendrites can be basal and oblique dendrites of layer 2 pyramidal neurons, or intermediate and terminal dendrites of layer 3 and 5 pyramidal neurons (*45, 46*). Among the non pyramidal inhibitory neurons in layer 2, Martinotti cells have the highest number of dendritic spines (*47*), but spine density is at least one third lower in these cells than in pyramidal neurons (*47*). Thus, to make sure that our analysis was restricted to pyramidal cells we avoided all dendritic segments with few or no spines.

All protrusions were defined as "spines" (as suggested in (*3*)), and divided in spines with synapses and spines lacking synapses (~13% of all protrusions; Table S1). A synapse was defined by the presence of a presynaptic bouton with at least 2 synaptic vesicles within a 50 nm distance from the cellular membrane facing the spine, a visible synaptic cleft and a postsynaptic density. In total, 101 dendritic branches were segmented in M1 ~30/group), and 67 in S1 (~20/group). Distribution of dendritic diameters was balanced across experimental groups (Fig. S2) and all segmentation data were tested for accuracy and consistency by the same experienced tracer (LdV).

The axon-spine interface (ASI) was traced at the interface between the spine head and the presynaptic terminal or bouton, and computed as described in (*48*). Specifically the region of contact between the two apposed objects was outlined in each individual section using the arealist brush suitably set at 1 pixel size. In this way, a quasi two-dimensional sheet-like object representing the interfaced region was created along the z dimension. The total surface area was calculated by computing the smoothed upper bound surface, according to the formula

$$Smoothed\ upper\ bound\ surface\ = \sum_{k=0}^{n} \left(P_s(a)\times\frac{1}{2}T\right) + \left(P_s(b)\times\frac{1}{2}T\right) + [A\ (a) - A(b)]$$

where n is the number of sections, a and b are the traced elements at the top and bottom of a section k of thickness T, Ps is the smoothed perimeter, and A is the area (*44*). Finally, the area of the traced element in the section k=1 and in the section k=n were subtracted from the smoothed upper bound surface value and the result was divided by 2 to get an approximate value of the apposed surface (AS). To validate this approach, AS values of 20 apposed elements were also calculated using the profile tool that

allows to trace one-dimensional lines along the contact region between two elements in each individual section. By doing so, the surface area is then computed by summing up the length of all the lines and multiplying this value by the thickness of the section (*49*). Quantitative analysis showed that the two methods lead to similar results, with a mean difference of 3.7%. However, the latter approach, albeit extensively used (*49, 50*), does not take into account possible changes in the size of elements within single sections, and therefore can be less precise than the smoothed upper bound surface. Moreover, segmenting AS with the area lists brush is faster and easier than using the profile tool. Thus, all the interfacing surfaces were segmented using the area lists brush and estimated according to the smoothed upper bound formula. ASI was not segmented in a subset of "oblique" spines (~10% in each stack, across all 3 groups) whose synapses were oriented obliquely or orthogonally to the cutting plane. The presence/absence of the following structures was recorded for each spine: spine apparatus, spinulae in the head or neck of the spine, mitochondria in the presynaptic element, and components of the non-smooth endoplasmic reticulum (non-SER). Non-SER elements were classified according to (*20*); they are spine organelles distinct from the continuous network of smooth endoplasmic reticulum (SER) present throughout the dendritic shaft, and include tubules, small uncoated vesicles, large coated or uncoated vesicles, and multivesicular bodies (MVBs). Small uncoated vesicles are considered of exosomal origin, while all other non-SER elements are likely recycling endosomes (*20*). Mitochondria were always present along the dendrites but very rarely found inside dendritic spines, consistent with previous reports (*51, 52*).

Statistical analysis. Repeated measures occur when multiple observations are drawn from the same experimental unit. Under these circumstances, many of the common statistical techniques are not valid because they violate independence assumptions. Tools to analyze repeated measures data include the repeated measures ANOVA and a linear mixed effect (LME) model, in which the experimental units are treated as random effects in the model. LME models offer several advantages over repeated measures ANOVA including - crucial in our study - the ability to handle unbalanced designs and missing data, as well as great flexibility with post-hoc tests.

Statistical analysis was performed using a LME model that includes both random and fixed effects. In the current work, we focused on LMEs of the form

$$Y_{i,j,k} = \beta_0 + b_j + b_k + \sum_{p=1}^{P} \beta_p X_{i,j,k,p} + \epsilon_{i,j,k}$$

where,

$$b_{0,j} \sim N(0, \sigma^2_{mouse}),$$

$$b_{0,k} \sim N(0, \sigma^2_{dendrite}),$$

$$b_{0,j} \perp b_{0,k}$$

and

$$\epsilon_{i,j,k} \sim N(0, \sigma^2).$$

In this model, $Y_{i,j,k}$ is the response variable, either the log(ASI) or log(HV) values, of the i^{th} observation from the j^{th} mouse and the k^{th} dendrite. The values $b_{0,j}$ and $b_{0,k}$ values are the random intercepts for each individual mouse and dendrite, respectively. The random intercepts are assumed to be independent and normally distributed, with mean zero and constant variance. The β values correspond to the fixed effects in the model, β_0 is the model intercept, and β_p the effect of the p^{th} explanatory variable. The design matrix X contains the values for each explanatory variable. The residuals $\epsilon_{i,j,k}$ are assumed to be independent and normally distributed with constant variance.

Model selection was performed using the Akaike Information Criterion (AIC), a procedure that balances the value of the likelihood against the number of parameters in the model to avoid over / under fitting. Alternative model selection procedures, such as stepwise inclusion / exclusion were also investigated, but they had minimal effect on the outcome. Parameter estimation of LMEs was performed using numerical maximum likelihood estimators, implemented in R by the lmer() function of the lme4 package.

Linear Mixed Effect Model – ASI

The optimal fixed effects model for the log(ASI) included condition and dendrite diameter (see Table below).

Table: LME for log(ASI)

Random Effects	**Standard Error**		
Dendrite (Intercept)	0.1041		
Mouse (Intercept)	0.0655		
Residual	0.9555		
Fixed Effects	**Level**	**Estimate**	**Standard Error**
Intercept		-1.9776	0.0688
Condition	Sleep (reference)	0	0
	Spontaneous Wake	0.2095	0.0587

	Enforced Wake	0.1928	0.0590
Diameter		0.00013	0.00006

Residual plots (shown below, left) were used to assess the model assumptions of normality and constant variance. From the scatter plot of residuals vs. fitted values, we found no evidence against the assumption of constant variance. From the qq-plot (shown below, middle), we saw a slight departure from normality in the tails of the distribution: the distribution was still symmetric but the tails were 'lighter' than a normal distribution. The LME estimates were robust to departures from normality (*53*), and given the mild deviation from normality, we were satisfied that the results were accurate. Density estimates (shown below, right), were used to assess normality and variance for each mouse.

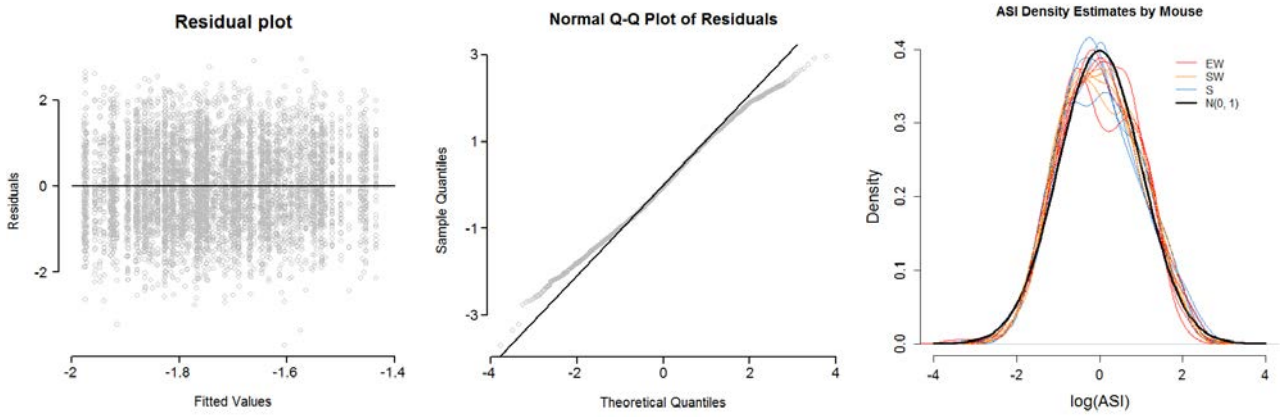

Diagnostic plots for LME model of ASI. Left: Scatter plot of estimated residuals against fitted values to evaluate homogenous variance. Middle: qq-plot of estimated residuals to assess normality. Right: Density estimates for each individual mouse to show normality (black line) and constant variance, and to rule out outliers.

To test the significance of condition in our model, we performed a likelihood ratio test against a reduced model condition removed. The results demonstrated strong evidence of a condition effect ($\chi^2 = 10.159$, df = 2, p-value = 0.0062). Post-hoc tests of the effect of condition found strong evidence that the average log(ASI) value is lower in S than in SW and EW, and no significant difference was found between SW and EW (see main text and Fig. 2).

Finally, we further analyzed our data to determine the potential interaction of three different organelles with the condition effect (spine apparatus, vesicles/tubules/MVBs, axonal mitochondria; see main text, Fig. 3) as well as two other biological features (synapse size, spine density). To test for an interaction with condition, we fit additional models with a variable by condition interaction, and then tested the significance of the interaction term using a likelihood ratio test. We found no significant interaction

between condition and brain region ($\chi^2 = 1.9745$, df = 2, p = 0.3726), dendrite diameter ($\chi^2 = 3.8865$, df = 2, p = 0.1432), spine apparatus ($\chi^2 = 3.1552$, df = 2, p = 0.2065) or axonal mitochondria ($\chi^2 = 1.0472$, df = 2, p = 0.5924), but did find strong evidence for a vesicles/tubules/MVBs by condition interaction ($\chi^2 = 20.811$, df = 2, p = 0.00003). We then further explored the condition by vesicles/tubules/MVBs interaction using post-hoc tests. The spines with vesicles/tubules/MVBs replicated the findings from the initial model, while we found no significant condition differences in the group of spines without vesicles/tubules/MVBs (see main text and Fig. 3). We found a significant interaction between spine density and condition ($\chi^2 = 6.535$, df = 2, p = 0.0381), with scaling being strongest for synapses on sparse dendrites, and the effect decreasing for synapses on densely packed dendrites. Lastly, to test for an interaction with synaptic size, we defined a categorical variable for synaptic size (small, large) by dividing the population of synapses into the smallest 80% of ASI values and the largest 20% of ASI values. The interaction with synaptic size was significant ($\chi^2 = 9.4296$, df = 2, p = 0.009). Post-hoc tests revealed that the small synapses scaled across conditions, but the large synapses had no significant differences (see main text and Fig. 3). The choice of an 80/20 split for small/large synapses was based on the scaling models presented in Fig. 2 and a binned analysis of scaling by synaptic size (see below, right), but it was a subjective choice of threshold. Thus, we performed a sensitivity analysis to determine if the results were influenced by the decision. From the analysis (see below, left), it is clear that the results are not sensitive to the specific choice of threshold, and that similar results would be found if the threshold was selected in a broader range (0.65- 0.9).

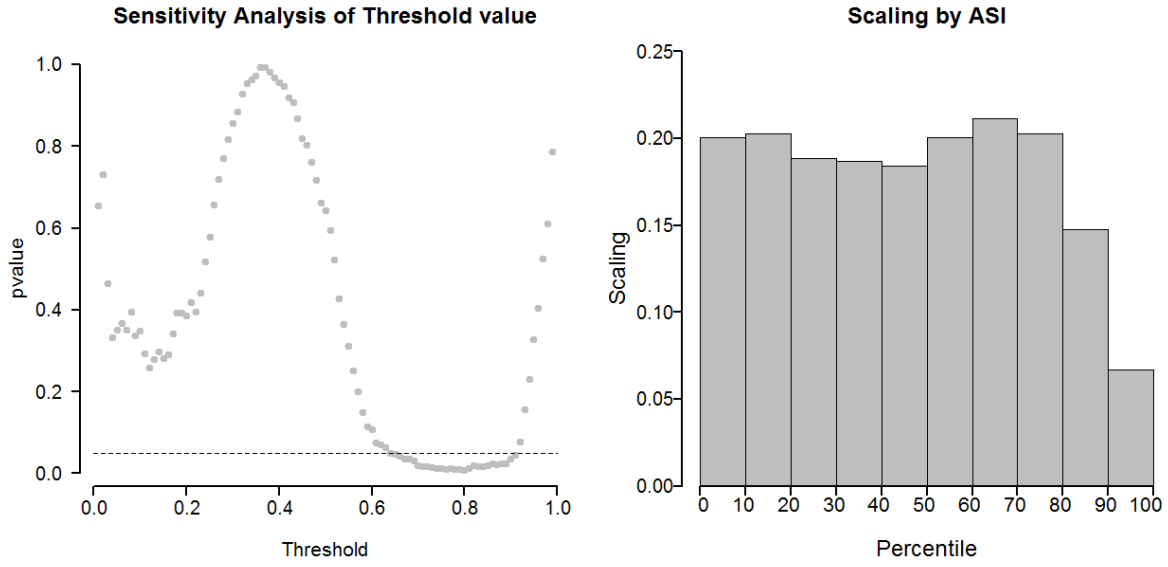

Size dependent scaling. Left: A sensitivity analysis demonstrates that the interaction between synapse size and scaling is not sensitive to the choice of cutoff threshold. Similar statistical significance is achieved for thresholds in the 0.7-0.9 range. Right:

Binned distribution of scaling as a function of synapse size. Scaling fluctuates around 0.2 for the bottom 80% of ASI values, then decreases for the greatest 20%.

Scaling analysis. To assess the presence of a scaling relationship, we tested the hypothesis that two probability distributions on a log scale differ only by a location shift. That is, we tested the hypothesis H_0: $f_1(x) = f_2(x - c)$. To do this, we first estimated c as the difference in the median of the two distributions, transformed the data so that under the null hypothesis they will have the same distribution, and then applied the Kolmogorov-Smirnov test for equality of distribution between two samples. Comparing the S and SW synapses gave an estimated shift of c = -0.225, corresponding to a scaling to -20.1% of the original value, and the KS test found no evidence against the hypothesis of scaling (D = 0.020, p = 0.784). Similarly, when we compared EW and S, we obtained an estimated shift of c = -0.212 or scaling to -19.1%, with no evidence against the null hypothesis (D = 0.023, p = 0.648).

Scaling Models. Finally, we explored three potential scaling models to determine the best fit for our data: uniform scaling, selective scaling and size-dependent scaling. In the uniform scaling model, every synapse is scaled down by the same amount. In the selective scaling model, a proportion of synapses are randomly selected to be "protected" (not scaled) and the rest are scaled by a fixed amount. In the size-dependent model, a proportion of the synapses are randomly selected to be protected, with the likelihood of being protected increasing quadratically with synaptic strength (ASI size). For each model the magnitude of scaling was adjusted so that the average scaling across all synapses was equal across models.

To assess the goodness of each model, the EW and SW conditions were combined to create a single population of wake (W) synapses. A Monte Carlo procedure was used to estimate the mean squared error (MSE = bias squared + variance) of estimating the evidence against a scaling hypothesis (p-value from the Kolmogorov-Smirnov test). Synapses from the W population were randomly sampled with replacement to create bootstrapped samples of the W population, a scaling procedure was applied to the W samples to generate bootstrapped samples from the S population, and then we tested for a scaling relationship between the bootstrapped W and S datasets. This process was repeated n = 5000 times for each model to estimate its MSE. The uniform model had a MSE of 0.22, the selective scaling model reached a minimum MSE of 0.05 when 50% of synapses were scaled, and the size-dependent model had the lowest MSE of 0.02 when 87% of synapses scaled (see main text, Fig. 2D). Overall, the size-dependent selective scaling model provided the best fit for our data.

Linear Mixed Effect Model – Head Volume

The optimal fixed effects model for the log(HV) included condition, brain region and dendrite diameter, as well as a condition by brain region interaction and a condition by diameter interaction (see Table below).

Table: LME for log(HV)

Random Effects	**Standard Error**		
Dendrite (Intercept)	0.1177		
Mouse (Intercept)	0.0670		
Residual	0.8444		
Fixed Effects	**Level**	**Estimate**	**Standard Error**
Intercept		-2.511	0.1003
Dendrite Diameter		0.00008	0.00010
Condition	Sleep (reference)	0	0
	Spontaneous Wake	-0.0036	0.1440
	Enforced Wake	-0.1990	0.1527
Brain region	S1 (reference)	0	0
	M1	0.1427	0.0499
Condition x Diameter	Sleep (reference)	0	0
	Spontaneous Wake	0.0003	0.0001
	Enforced Wake	0.0004	0.0002
Condition x Brain region	S1, Sleep (reference)	0	0
	M1, Spont. Wake	-0.1447	0.0701
	M1, Enforced Wake	-0.0494	0.0705

Residual plots (shown below, left) were used to assess the model assumptions of normality and constant variance. From the scatter plot of residuals vs. fitted values, and the qq-plot of residual (shown below, middle), we found no evidence against the assumptions of constant variance and normality, outside of a handful of outliers at the lower end of the distribution. Density estimates (shown below, right), were used to assess normality and variance for each mouse.

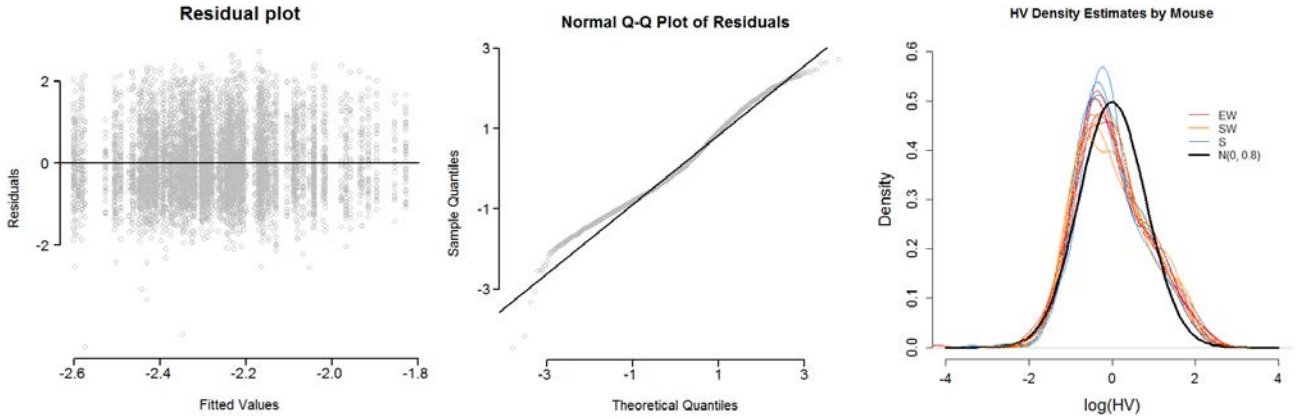

Diagnostic plots for LME model of HV. Left: Scatter plot of estimated residuals against fitted values to evaluate homogenous variance. Middle: qq-plot of estimated residuals to assess normality. Right: Density estimates for each individual mouse to show normality (black line) and constant variance, and to rule out outliers.

To test the significance of condition in our model, we performed a likelihood ratio test against a reduced model with the interaction removed. We found no significant effect for the condition by brain region interaction (χ^2 = 4.312, df = 2, p = 0.1158), and evidence for a significant condition by diameter interaction (χ^2 = 6.942, df = 2, p = 0.0311). Post-hoc analysis found that the effect of condition was as follows: Sleep has reduced HV when compared to SW and EW, and this effect was strongest for high diameter dendrites (Fig. S3).

Finally, as for the ASI we further analyzed HV to determine the potential interaction of three different organelles with the condition effect (spine apparatus, vesicles/tubules/MVBs, axonal mitochondria; see Fig. S3) as well as spine size and spine density. We found no significant interaction between condition and spine apparatus (χ^2 = 1.2483, df = 2, p = 0.5357), axonal mitochondria (χ^2 = 5.8061, df = 2, p = 0.0549), spine size (χ^2 = 0.0912, df = 2, p = 0.9554) or spine density (χ^2 = 2.3881, df = 2, p = 0.3030) but did find strong evidence for a vesicles/tubules/MVBs by condition interaction (χ^2 = 31.962, df = 2, p = 0.0000001). We then further explored the condition by vesicles/tubules/MVBs interaction: the group of spines with vesicles/tubules/MVBs replicated the findings from the initial model, while there were no condition differences in the group of spines without vesicles/tubules/MVBs (Fig. S3).

Fig. S1. 3D Reconstruction of all dendritic segments used in the study. Scale bar = 25 μm.

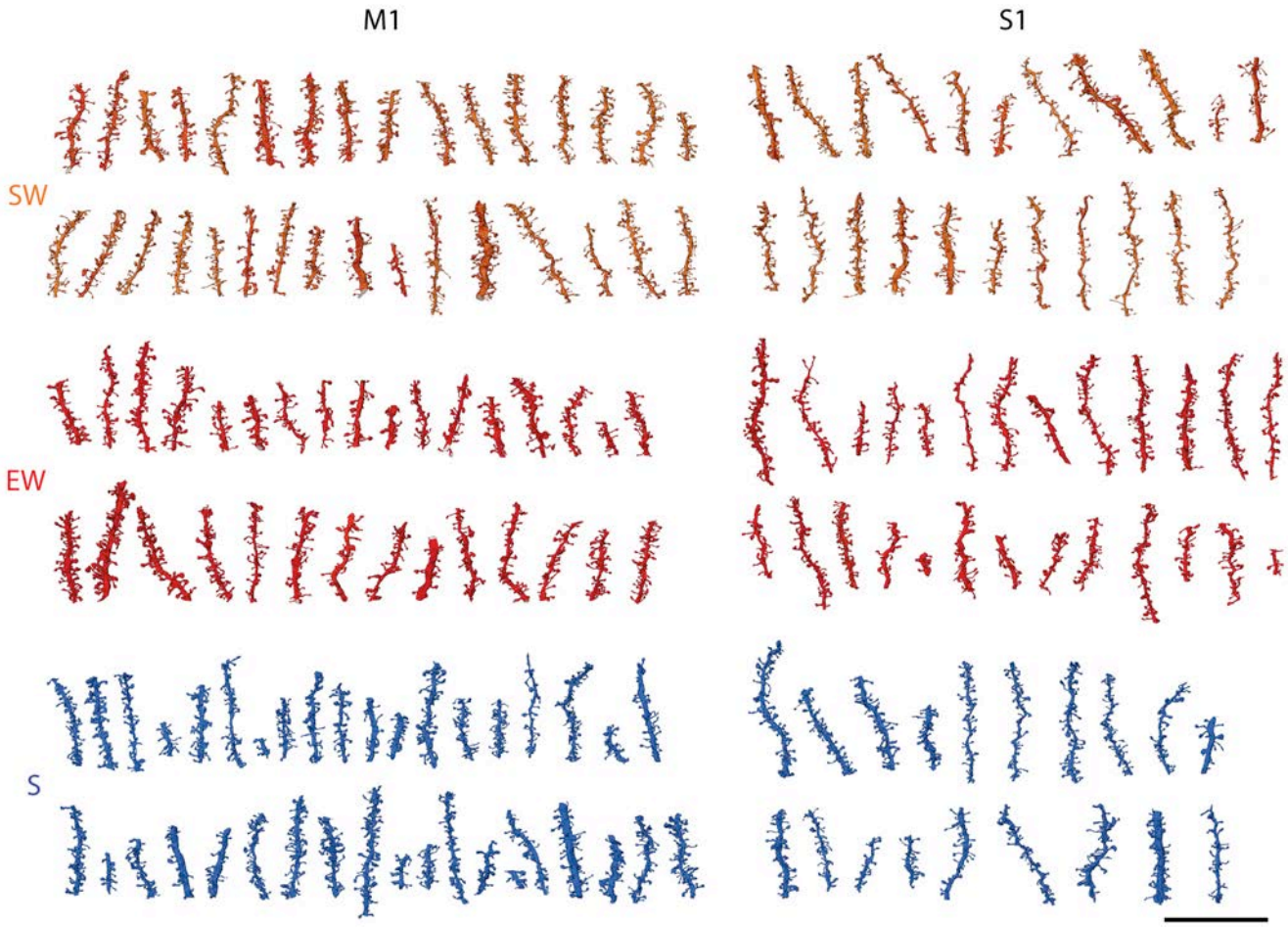

Fig. S2. Distribution of mitochondrial and dendrite diameters across groups. The LME models include condition and region as fixed effects and mouse as a random effect: there is no significant effect of condition for either the mitochondrial diameter (p = 0.445) or the dendrite diameter (p = 0.248). The figure also shows the p-values for the pairwise comparisons between groups.

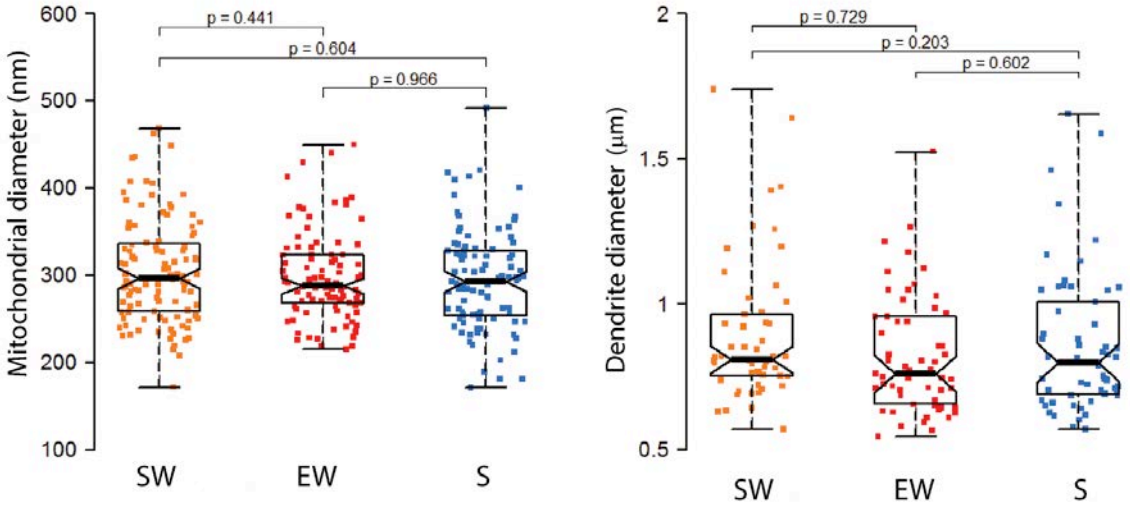

Fig. S3. HV decreases in sleep. A, HV of all spines, each represented by one dot. **B**, the effect of sleep on HV interacts with the effect of dendrite diameter, with the largest decline occurring in the biggest dendrites. At the average value of dendrite diameter (vertical line; 0.86 μm), the mean overall decrease is -12.1% (S vs. SW, -12.8%, p = 0.0488; S vs. EW, -11.2%, p = 0.1043). **C**, log-normal distribution of HV in the 3 experimental groups. **D**, the HV decline during sleep is significant in the group of spines with non-SER components (vesicles, tubules, and multivesicular bodies, labeled "vesicles/tubules"). **E**, the HV decrease during sleep in spines with vesicles/tubules is due to scaling. * p<0.05; *** p<0.001.

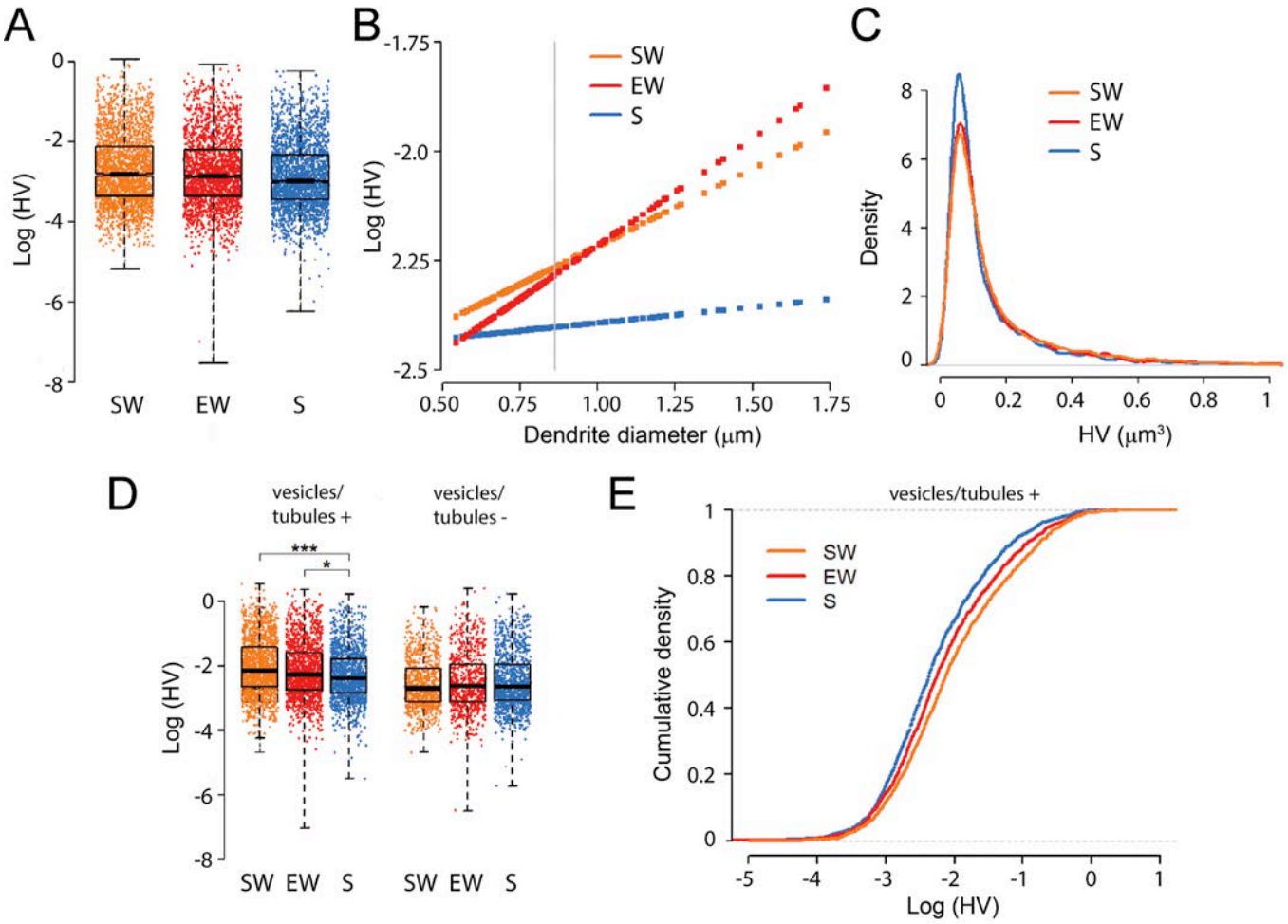

Table S1. Summary of ultrastructural measures. All protrusions are defined as spines. In oblique spines the ASI could not be measured because the synapse was oriented obliquely or orthogonally to the cutting plane.

	M1			S1		
	SW	EW	S	SW	EW	S
Total N of dendrites = 168	32	31	38	22	26	19
Total N of spines = 8,427	1752	1480	1810	1167	1136	1082
Total N of spines with synapse (some incomplete) = 7,149	1521	1306	1521	946	961	894
Total N of measured spines with synapse (oblique included; used for HV analysis) = 6,920	1461	1256	1486	913	923	881
Total N of measured spines with synapse (oblique excluded; used for ASI analysis) = 6,305	1341	1153	1344	839	836	792
Head volume (μm^3, mean±std) range (μm^3)	0.164±0.183 0.017-1.746	0.166±0.191 0.010-1.522	0.144±0.156 0.003-1.292	0.165±0.171 0.009-1.293	0.145±0.143 0.001-1.022	0.126±0.131 0.004-0.821
Total N of ASIs measured	1341	1153	1344	839	836	792
ASI (μm^2, mean±std) range (μm^2)	0.301±0.339 0.012-4.019	0.294±0.324 0.007-3.543	0.256±0.289 0.010-2.038	0.297±0.297 0.013-2.061	0.284±0.275 0.005-1.610	0.234±0.257 0.006-1.938
Spine density (all protrusions) (#/μm^2, mean±std)	0.78±0.22	0.82±0.24	0.83±0.24	0.70±0.23	0.70±0.20	0.81±0.22
Density of spines with synapse (#/μm^2, mean±std)	0.68±0.19	0.72±0.24	0.68±0.20	0.56±0.18	0.59±0.17	0.66±0.18
Density of spines without synapse (#/μm^2, mean±std)	0.09±0.06	0.08±0.04	0.10±0.06	0.11±0.07	0.09±0.06	0.11±0.06
Oblique spines (% of complete spines with synapse, mean±std)	8.8±2.8	8.5±1.2	9.7±0.6	8.2±1.2	13.1±4.5	10.2±2.4
Spines without synapse (%, mean±std)	12.3±6.0	10.5±5.5	12.7±6.2	16.9±7.6	12.8±6.8	14±5.6
Dendrite diameter (µm, mean±std)	0.89±0.25	0.84±0.22	0.86±0.23	0.90±0.24	0.79±0.18	0.86±0.27
Dendrite length (µm, mean±std)	26±5	22±6	22±8	28±7	26±9	27±8
Incomplete spines (go off the image) (%, mean±std)	1.32±1.51	2.02±1.96	3.67±4.29	2.99±2.72	3.51±7.06	4.39±4.45
Spines with spine apparatus (% per mouse, mean±std)	30.47±4.37	27.00±3.08	26.13±4.33	29.66±3.56	31.31±1.60	26.14±4.60
Spines with non-SER elements (tubules/vesicles/MVBs; % per mouse, mean±std)	56.33±12.92	61.22±7.02	49.74±6.93	74.18±8.95	73.10±8.93	65.19±12.30
Synapses with mitochondrion in the axonal bouton (% per mouse, mean±std)	32.99±5.11	33.03±2.79	32.46±2.84	36.45±3.06	37.15±0.84	34.94±3.75

Table S2. **Average percentage of spines with special anatomical features**. All values represent mean ± std.

	M1			S1		
	SW	**EW**	**S**	**SW**	**EW**	**S**
% of spines with coated vesicles in the head/neck	2.02 ± 1.24	6.61 ± 3.87	3.17 ± 2.16	3.05 ± 2.30	1.99 ± 2.44	2.00 ± 1.12
% of spines with a spinula	1.11 ±0.53	1.36 ± 1.63	1.32 ± 0.69	2.30 ± 2.84	1.16 ± 1.00	0.79 ± 0.20
% of spines with a MVB in head/ neck/base	3.99 ± 1.66	7.78 ± 3.89	2.79 ± 1.60	8.71 ± 4.62	5.46 ± 1.48	3.75 ± 2.75
% of branched spines	17.1 ± 5.27	14.2 ±3.7	15.8 ± 3.2	10.6 ± 6.9	10.2 ± 2.6	11.5 ± 2.9

References and Notes

1. S. Herculano-Houzel, The human brain in numbers: A linearly scaled-up primate brain. *Front. Hum. Neurosci.* **3**, 31 (2009). Medline doi:10.3389/neuro.09.031.2009

2. Y. Tang, J. R. Nyengaard, D. M. De Groot, H. J. Gundersen, Total regional and global number of synapses in the human brain neocortex. *Synapse* **41**, 258–273 (2001). Medline doi:10.1002/syn.1083

3. A. Holtmaat, K. Svoboda, Experience-dependent structural synaptic plasticity in the mammalian brain. *Nat. Rev. Neurosci.* **10**, 647–658 (2009). Medline doi:10.1038/nrn2699

4. J. Nishiyama, R. Yasuda, Biochemical computation for spine structural plasticity. *Neuron* **87**, 63–75 (2015). Medline doi:10.1016/j.neuron.2015.05.043

5. K. M. Harris, J. K. Stevens, Dendritic spines of CA 1 pyramidal cells in the rat hippocampus: Serial electron microscopy with reference to their biophysical characteristics. *J. Neurosci.* **9**, 2982–2997 (1989). Medline

6. N. L. Desmond, W. B. Levy, Synaptic interface surface area increases with long-term potentiation in the hippocampal dentate gyrus. *Brain Res.* **453**, 308–314 (1988). Medline doi:10.1016/0006-8993(88)90171-0

7. P. A. Buchs, D. Muller, Induction of long-term potentiation is associated with major ultrastructural changes of activated synapses. *Proc. Natl. Acad. Sci. U.S.A.* **93**, 8040–8045 (1996). Medline doi:10.1073/pnas.93.15.8040

8. C. E. Cheetham, S. J. Barnes, G. Albieri, G. W. Knott, G. T. Finnerty, Pansynaptic enlargement at adult cortical connections strengthened by experience. *Cereb. Cortex* **24**, 521–531 (2014). Medline doi:10.1093/cercor/bhs334

9. Y. Katz, V. Menon, D. A. Nicholson, Y. Geinisman, W. L. Kath, N. Spruston, Synapse distribution suggests a two-stage model of dendritic integration in CA1 pyramidal neurons. *Neuron* **63**, 171–177 (2009). Medline doi:10.1016/j.neuron.2009.06.023

10. M. Matsuzaki, G. C. Ellis-Davies, T. Nemoto, Y. Miyashita, M. Iino, H. Kasai, Dendritic spine geometry is critical for AMPA receptor expression in hippocampal CA1 pyramidal neurons. *Nat. Neurosci.* **4**, 1086–1092 (2001). Medline doi:10.1038/nn736

11. M. Bosch, J. Castro, T. Saneyoshi, H. Matsuno, M. Sur, Y. Hayashi, Structural and molecular remodeling of dendritic spine substructures during long-term potentiation. *Neuron* **82**, 444–459 (2014). Medline doi:10.1016/j.neuron.2014.03.021

12. D. E. Feldman, Synaptic mechanisms for plasticity in neocortex. *Annu. Rev. Neurosci.* **32**, 33–55 (2009). Medline doi:10.1146/annurev.neuro.051508.135516

13. R. L. Huganir, R. A. Nicoll, AMPARs and synaptic plasticity: The last 25 years. *Neuron* **80**, 704–717 (2013). Medline doi:10.1016/j.neuron.2013.10.025

14. C. von der Malsburg, Self-organization of orientation sensitive cells in the striate cortex. *Kybernetik* **14**, 85–100 (1973). Medline doi:10.1007/BF00288907

15. M. Chistiakova, N. M. Bannon, J. Y. Chen, M. Bazhenov, M. Volgushev, Homeostatic role of heterosynaptic plasticity: Models and experiments. *Front. Comput. Neurosci.* **9**, 89 (2015). Medline doi:10.3389/fncom.2015.00089

16. G. Tononi, C. Cirelli, Sleep and the price of plasticity: From synaptic and cellular homeostasis to memory consolidation and integration. *Neuron* **81**, 12–34 (2014). Medline doi:10.1016/j.neuron.2013.12.025

17. B. Rasch, J. Born, About sleep's role in memory. *Physiol. Rev.* **93**, 681–766 (2013). Medline doi:10.1152/physrev.00032.2012

18. W. C. Abraham, A. Robins, Memory retention—The synaptic stability versus plasticity dilemma. *Trends Neurosci.* **28**, 73–78 (2005). Medline doi:10.1016/j.tins.2004.12.003

19. W. Denk, H. Horstmann, Serial block-face scanning electron microscopy to reconstruct three-dimensional tissue nanostructure. *PLOS Biol.* **2**, e329 (2004). Medline doi:10.1371/journal.pbio.0020329

20. J. R. Cooney, J. L. Hurlburt, D. K. Selig, K. M. Harris, J. C. Fiala, Endosomal compartments serve multiple hippocampal dendritic spines from a widespread rather than a local store of recycling membrane. *J. Neurosci.* **22**, 2215–2224 (2002). Medline

21. P. S. Holcomb, B. K. Hoffpauir, M. C. Hoyson, D. R. Jackson, T. J. Deerinck, G. S. Marrs, M. Dehoff, J. Wu, M. H. Ellisman, G. A. Spirou, Synaptic inputs compete during rapid formation of the calyx of Held: A new model system for neural development. *J. Neurosci.* **33**, 12954–12969 (2013). Medline doi:10.1523/JNEUROSCI.1087-13.2013

22. Y. Loewenstein, A. Kuras, S. Rumpel, Multiplicative dynamics underlie the emergence of the log-normal distribution of spine sizes in the neocortex in vivo. *J. Neurosci.* **31**, 9481–9488 (2011). Medline doi:10.1523/JNEUROSCI.6130-10.2011

23. M. Cane, B. Maco, G. Knott, A. Holtmaat, The relationship between PSD-95 clustering and spine stability in vivo. *J. Neurosci.* **34**, 2075–2086 (2014). Medline doi:10.1523/JNEUROSCI.3353-13.2014

24. M. Park, J. M. Salgado, L. Ostroff, T. D. Helton, C. G. Robinson, K. M. Harris, M. D. Ehlers, Plasticity-induced growth of dendritic spines by exocytic trafficking from recycling endosomes. *Neuron* **52**, 817–830 (2006). Medline doi:10.1016/j.neuron.2006.09.040

25. J. H. Tao-Cheng, V. T. Crocker, C. A. Winters, R. Azzam, J. Chludzinski, T. S. Reese, Trafficking of AMPA receptors at plasma membranes of hippocampal neurons. *J. Neurosci.* **31**, 4834–4843 (2011). Medline doi:10.1523/JNEUROSCI.4745-10.2011

26. A. J. Holtmaat, J. T. Trachtenberg, L. Wilbrecht, G. M. Shepherd, X. Zhang, G. W. Knott, K. Svoboda, Transient and persistent dendritic spines in the neocortex in vivo. *Neuron* **45**, 279–291 (2005). Medline doi:10.1016/j.neuron.2005.01.003

27. N. Holbro, A. Grunditz, T. G. Oertner, Differential distribution of endoplasmic reticulum controls metabotropic signaling and plasticity at hippocampal synapses. *Proc. Natl. Acad. Sci. U.S.A.* **106**, 15055–15060 (2009). Medline doi:10.1073/pnas.0905110106

28. L. E. Ostroff, C. K. Cain, J. Bedont, M. H. Monfils, J. E. Ledoux, Fear and safety learning differentially affect synapse size and dendritic translation in the lateral amygdala. *Proc. Natl. Acad. Sci. U.S.A.* **107**, 9418–9423 (2010). Medline doi:10.1073/pnas.0913384107

29. V. V. Vyazovskiy, C. Cirelli, M. Pfister-Genskow, U. Faraguna, G. Tononi, Molecular and electrophysiological evidence for net synaptic potentiation in wake and depression in sleep. *Nat. Neurosci.* **11**, 200–208 (2008). Medline doi:10.1038/nn2035

30. D. Bushey, G. Tononi, C. Cirelli, Sleep and synaptic homeostasis: Structural evidence in Drosophila. *Science* **332**, 1576–1581 (2011). Medline doi:10.1126/science.1202839

31. H. Makino, R. Malinow, Compartmentalized versus global synaptic plasticity on dendrites controlled by experience. *Neuron* **72**, 1001–1011 (2011). Medline doi:10.1016/j.neuron.2011.09.036

32. G. W. Knott, C. Quairiaux, C. Genoud, E. Welker, Formation of dendritic spines with GABAergic synapses induced by whisker stimulation in adult mice. *Neuron* **34**, 265–273 (2002). Medline doi:10.1016/S0896-6273(02)00663-3

33. G. H. Diering, A. S. Gustina, R. L. Huganir, PKA-GluA1 coupling via AKAP5 controls AMPA receptor phosphorylation and cell-surface targeting during bidirectional homeostatic plasticity. *Neuron* **84**, 790–805 (2014). Medline doi:10.1016/j.neuron.2014.09.024

34. G. Buzsáki, K. Mizuseki, The log-dynamic brain: How skewed distributions affect network operations. *Nat. Rev. Neurosci.* **15**, 264–278 (2014). Medline doi:10.1038/nrn3687

35. A. D. Grosmark, G. Buzsaki, Diversity in neural firing dynamics supports both rigid and learned hippocampal sequences. *Science* **351**, 1440–1443 (2016)..

36. L. de Vivo, U. Faraguna, A. B. Nelson, M. Pfister-Genskow, M. E. Klapperich, G. Tononi, C. Cirelli, Developmental patterns of sleep slow wave activity and synaptic density in adolescent mice. *Sleep* **37**, 689–700, 700A–700B (2014). Medline

37. A. B. Nelson, U. Faraguna, J. T. Zoltan, G. Tononi, C. Cirelli, Sleep patterns and homeostatic mechanisms in adolescent mice. *Brain Sci.* **3**, 318–343 (2013). Medline doi:10.3390/brainsci3010318

38. S. Maret, U. Faraguna, A. B. Nelson, C. Cirelli, G. Tononi, Sleep and waking modulate spine turnover in the adolescent mouse cortex. *Nat. Neurosci.* **14**, 1418–1420 (2011). Medline doi:10.1038/nn.2934

39. M. Bellesi, M. Pfister-Genskow, S. Maret, S. Keles, G. Tononi, C. Cirelli, Effects of sleep and wake on oligodendrocytes and their precursors. *J. Neurosci.* **33**, 14288–14300 (2013). Medline doi:10.1523/JNEUROSCI.5102-12.2013

40. V. V. Vyazovskiy, U. Olcese, E. C. Hanlon, Y. Nir, C. Cirelli, G. Tononi, Local sleep in awake rats. *Nature* **472**, 443–447 (2011). Medline doi:10.1038/nature10009

41. S. A. Wilke, J. K. Antonios, E. A. Bushong, A. Badkoobehi, E. Malek, M. Hwang, M. Terada, M. H. Ellisman, A. Ghosh, Deconstructing complexity: Serial block-face electron microscopic analysis of the hippocampal mossy fiber synapse. *J. Neurosci.* **33**, 507–522 (2013). Medline doi:10.1523/JNEUROSCI.1600-12.2013

42. J. Schindelin, I. Arganda-Carreras, E. Frise, V. Kaynig, M. Longair, T. Pietzsch, S. Preibisch, C. Rueden, S. Saalfeld, B. Schmid, J. Y. Tinevez, D. J. White, V. Hartenstein, K. Eliceiri, P. Tomancak, A. Cardona, Fiji: An open-source platform for biological-image analysis. *Nat. Methods* **9**, 676–682 (2012). Medline doi:10.1038/nmeth.2019

43. J. C. Fiala, K. M. Harris, Cylindrical diameters method for calibrating section thickness in serial electron microscopy. *J. Microsc.* **202**, 468–472 (2001). Medline doi:10.1046/j.1365-2818.2001.00926.x

44. A. Cardona, S. Saalfeld, J. Schindelin, I. Arganda-Carreras, S. Preibisch, M. Longair, P. Tomancak, V. Hartenstein, R. J. Douglas, TrakEM2 software for neural circuit reconstruction. *PLOS ONE* **7**, e38011 (2012). Medline doi:10.1371/journal.pone.0038011

45. K. I. van Aerde, D. Feldmeyer, Morphological and physiological characterization of pyramidal neuron subtypes in rat medial prefrontal cortex. *Cereb. Cortex* **25**, 788–805 (2015). Medline doi:10.1093/cercor/bht278

46. A. U. Larkman, Dendritic morphology of pyramidal neurones of the visual cortex of the rat: I. Branching patterns. *J. Comp. Neurol.* **306**, 307–319 (1991). Medline doi:10.1002/cne.903060207

47. Y. Kawaguchi, F. Karube, Y. Kubota, Dendritic branch typing and spine expression patterns in cortical nonpyramidal cells. *Cereb. Cortex* **16**, 696–711 (2006). Medline doi:10.1093/cercor/bhj015

48. M. Bellesi, L. de Vivo, G. Tononi, C. Cirelli, Effects of sleep and wake on astrocytes: Clues from molecular and ultrastructural studies. *BMC Biol.* **13**, 66 (2015). Medline doi:10.1186/s12915-015-0176-7

49. J. C. Fiala, Reconstruct: A free editor for serial section microscopy. *J. Microsc.* **218**, 52–61 (2005). Medline doi:10.1111/j.1365-2818.2005.01466.x

50. M. R. Witcher, S. A. Kirov, K. M. Harris, Plasticity of perisynaptic astroglia during synaptogenesis in the mature rat hippocampus. *Glia* **55**, 13–23 (2007). Medline doi:10.1002/glia.20415

51. G. W. Knott, A. Holtmaat, L. Wilbrecht, E. Welker, K. Svoboda, Spine growth precedes synapse formation in the adult neocortex in vivo. *Nat. Neurosci.* **9**, 1117–1124 (2006). Medline doi:10.1038/nn1747

52. N. Kasthuri, K. J. Hayworth, D. R. Berger, R. L. Schalek, J. A. Conchello, S. Knowles-Barley, D. Lee, A. Vázquez-Reina, V. Kaynig, T. R. Jones, M. Roberts, J. L. Morgan, J. C. Tapia, H. S. Seung, W. G. Roncal, J. T. Vogelstein, R. Burns, D. L. Sussman, C. E. Priebe, H. Pfister, J. W. Lichtman, Saturated reconstruction of a volume of neocortex. *Cell* **162**, 648–661 (2015). Medline doi:10.1016/j.cell.2015.06.054

53. G. Verbeke, E. Lesaffre, The effect of misspecifying the random-effects distribution in linear mixed models for longitudinal data. *Comput. Stat. Data Anal.* **23**, 541–556 (1997). doi:10.1016/S0167-9473(96)00047-3